

## 7-1 The Structure and Function of Histone Chaperone CIA Complexed with Histones H3 and H4

In eukaryotic cell nuclei, DNA is compacted into chromatin fibers. The chromatin fibers are composed of repetitive units, the nucleosomes, which are comprised of an octamer of two copies each of the four core histones, namely H2A, H2B, H3, and H4, and double stranded DNA. The crystal structure of the nucleosome core particle [1] reveals that one histone (H3-H4)<sub>2</sub> tetramer is flanked by two histone H2A-H2B dimers, forming a core histone octamer, and 146 bp of DNA is wrapped around the histone octamer. Although the nucleosome is important for compacting the DNA, the nucleosome must be disassembled during transcription, replication, and DNA-repair in order to allow reactions between the protein factors and naked DNA to proceed. Nucleosome assembly and disassembly are therefore essential for nuclear events in all eukaryotes. Since histone chaperones mediate the nucleosome assembly and disassembly, they have attracted the attention of researchers. Although the crystal structures of several histone chaperones have been determined, the molecular mechanism of nucleosome assembly and disassembly has remained elusive due to the lack of the three-dimensional structure of the histone chaperone-histone complex.

CIA (CCG1-interacting factor A) is the most conserved histone chaperone among the eukaryotes, and is involved in transcription, replication, and DNA-repair. Biochemical studies have revealed that CIA preferentially binds histone H3-H4, and has both nucleosome assembly and disassembly activities. In order to understand the mechanisms of nucleosome assembly and disassembly by CIA, we have determined the crystal structure of the CIA-histone-H3-H4 complex at 2.7 Å resolution using diffraction data collected at AR-NW12A [2]. The structure shows the histone H3-H4 dimer's mutually exclusive interactions with another histone H3-H4 dimer and CIA (Figs. 1a, 1b). Since the complex was crystallized by mixing of the histone (H3-H4)<sub>2</sub> tetramer and CIA, CIA is likely to have a histone (H3-H4)<sub>2</sub> tetramer disrupting activity. Biochemical analysis also demonstrated that CIA can disrupt the histone (H3-H4)<sub>2</sub> tetramer into two histone H3-H4 dimers through the formation of two CIA-histone-H3-H4 hetero-trimers (Fig. 1c). It is intriguing to note that the C-terminal β-strand of histone H4 changes its partner from the β-strand in histone H2A to that of CIA to form a new anti-parallel β-sheet through a large conformational change. Since

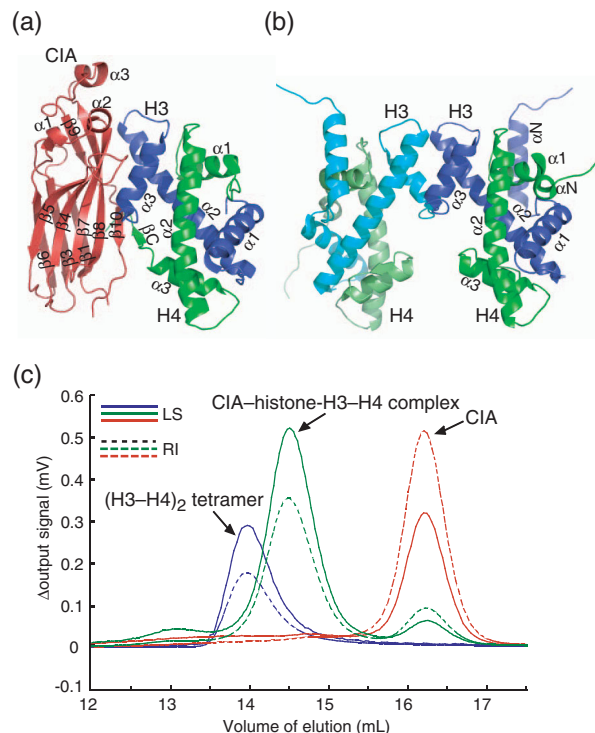
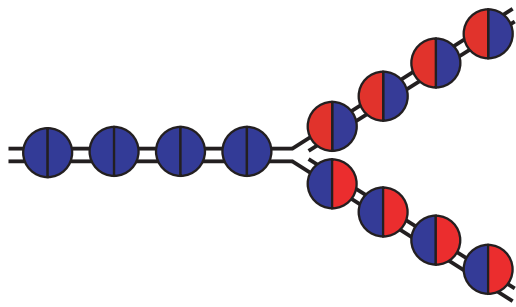




Figure 1

The mutually exclusive interaction of the histone H3-H4 dimer with another histone H3-H4 dimer and CIA. (a) Overall structure of the CIA-histone-H3-H4 complex. (b) Histone (H3-H4)<sub>2</sub> tetramer in the nucleosome core [1]. (c) Chromatograms of the histone (H3-H4)<sub>2</sub> tetramer, CIA, and the CIA-histone-H3-H4 complex are shown in blue, red and green, respectively. The solid and dashed lines represent output intensities from static light scattering (LS) and the differential refractometer (RI), respectively. The molecular weights of the histone (H3-H4)<sub>2</sub> tetramer, CIA and the CIA-histone-H3-H4 complex were estimated from the LS to RI ratios to be 53,910 ± 1,050 Da (theoretical value = 53,012 Da), 20,170 ± 30 Da (theoretical value = 19,812 Da) and 47,940 ± 70 Da (theoretical value = 46,318 Da), respectively. The addition of CIA to a histone (H3-H4)<sub>2</sub> tetramer causes it to disassociate into two histone H3-H4 dimers and form a CIA-histone-H3-H4 complex.

this small interaction seems to induce a large effect – the disruption of the histone H3-H4 tetramer by CIA, we describe the way for disruption as a “yawara split” following the spirit of Judo (Ju yoku go wo seisu – “softness tames toughness”). A comprehensive *in vivo* mutational analysis using *Saccharomyces cerevisiae* revealed that mutations of the residues located at the interface between CIA and histone H3 showed the SPT(-) phenotype, suggesting that the interaction observed in the crystal structure is of biological significance. In addition, the histone (H3-H4)<sub>2</sub> tetramer-disrupting activity of CIA and the crystal structure of the CIA-histone-H3-H4 complex give insights into semi-conservative nucleosome replication (Fig. 2). If nucleosomes are replicated in a semi-conservative manner, the epigenetic histone modifications of parental nucleosomes can be equally inherited to both of the two daughter nucleosomes.



-  parental histone H3-H4 dimer
-  newly synthesized histone H3-H4 dimer

**Figure 2**  
The semi-conservative nucleosome replication model. At the replication fork, the histone (H3-H4)<sub>2</sub> tetramer is disrupted into two histone H3-H4 dimers, each of which is delivered to each of the two daughter DNA strands. The daughter nucleosome is assembled with one parental H3-H4 dimer and one newly synthesized H3-H4 dimer. This model may provide a possible solution to the problem of epigenetic inheritance. The present result is the first experimental support for the nucleosome semi-conservative replication model.

**R. Natsume<sup>1</sup>, M. Eitoku<sup>2</sup>, Y. Akai<sup>1</sup>, N. Sano<sup>2</sup>, M. Horikoshi<sup>2,3</sup> and T. Senda<sup>4</sup>** (<sup>1</sup>JBIC-JBIRC, <sup>2</sup>IMCB, The Univ. of Tokyo, <sup>3</sup>JST-ERATO, <sup>4</sup>AIST)

#### References

- [1] K. Luger, A.W. Mäder, R.K. Richmond, D.F. Sargent and T.J. Richmond, *Nature*, **389** (1997) 6648.
- [2] R. Natsume, M. Eitoku, Y. Akai, N. Sano, M. Horikoshi and T. Senda, *Nature*, **446** (2007) 338.

## 7-2 Molecular Basis for Glu-tRNA<sup>Gln</sup>-Dependent Amidotransferase of Bacterial GatCAB

The pathway of glutamyl-tRNA<sup>Gln</sup> (Gln-tRNA<sup>Gln</sup>) synthesis is distinct among the three domains of life. In the eukaryotic cytoplasm, glutamyl-tRNA synthetase (GlnRS) produces Gln-tRNA<sup>Gln</sup> by attaching glutamine to tRNA<sup>Gln</sup> directly, whereas most bacteria and archaea do not have GlnRS and must utilize a tRNA-dependent transamidation pathway to synthesize Gln-tRNA<sup>Gln</sup>. In the first step of this pathway, mischarged Glu-tRNA<sup>Gln</sup> is synthesized by non-discriminating glutamyl-tRNA synthetase, which recognizes not only tRNA<sup>Glu</sup> but also tRNA<sup>Gln</sup>. The mischarged Glu-tRNA<sup>Gln</sup> is then transformed into the correctly charged Gln-tRNA<sup>Gln</sup> by Glu-tRNA<sup>Gln</sup>-dependent amidotransferase (Glu-AdT). Bacterial Glu-AdTs are heterotrimeric proteins composed of A, B, and C subunits, and are named GatCAB. GatCAB initially activates Glu-tRNA<sup>Gln</sup> by a kinase reaction in GatB at the expense of ATP. Subsequently, the activat-

ed Glu-tRNA<sup>Gln</sup> is transamidated into Gln-tRNA<sup>Gln</sup> using ammonia generated by a glutaminase reaction in GatA. These reactions are tightly coupled and dependent on the binding of Glu-tRNA<sup>Gln</sup>. However, very little is known about the detailed mechanism of this reaction coupling.

To further understand the mechanism in GatCAB, we initiated a crystal structure analysis of GatCAB from *Staphylococcus aureus*. The Se-SAD data set was collected to 2.8 Å resolution at BL41XU of the SPring-8 under cryogenic conditions (100 K). The native data set was collected to 2.5 Å resolution at AR-NW12A of the PF. The initial phases were improved by averaging over multiple crystals between Se-Met and the native crystal and extended to 2.5 Å, resulting in completion of the model building. Furthermore, we have determined the structures of GatCAB in the glutamine- and ADP-bound forms by soaking the crystals in a reservoir containing either 5 mM L-glutamine or 1 mM ADP [1].

The overall structure of GatCAB showed a unique subunit assembly (Fig. 3a). The interaction between GatA and GatB is strengthened by GatC, which wraps around the interface region of GatA and GatB as a molecular belt (Fig. 3b).

In the glutamine-binding structure, the glutamine was found at the center of GatA, interacting with the conserved Ser-*cis*-Ser-Lys catalytic triad: Ser178, *cis*-Ser154, and Lys79 (Fig. 3a and 4a). Surprisingly, a tetrahedral covalent intermediate was formed by the forming of a tight covalent bond between the side chain of Ser178 and the amide carbonyl carbon atom of the glutamyl side chain, indicating that the GatA catalytic center is actually in an active conformation even without Glu-tRNA<sup>Gln</sup> binding. Therefore, there is an unknown regulation of the glutaminase activity for the reaction coupling.

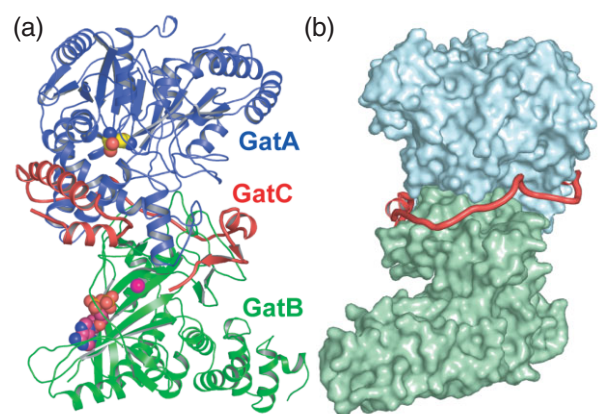


**Figure 3**  
(a) The overall structure of *S. aureus* GatCAB/glutamine complex, depicted in three different colors for each subunit; blue, green, and red for GatA, GatB, and GatC, respectively. The yellow spheres in the GatA model indicate glutamine binding to the active site of the glutaminase reaction. The magnesium ion at the active site of GatB is shown as a magenta sphere, and the pink spheres represent the ADP in the GatCAB/ADP complex. (b) The GatC molecular belt wrapping around the GatAB complex. GatA and GatB are shown as surfaces, and the red ribbon indicates GatC.

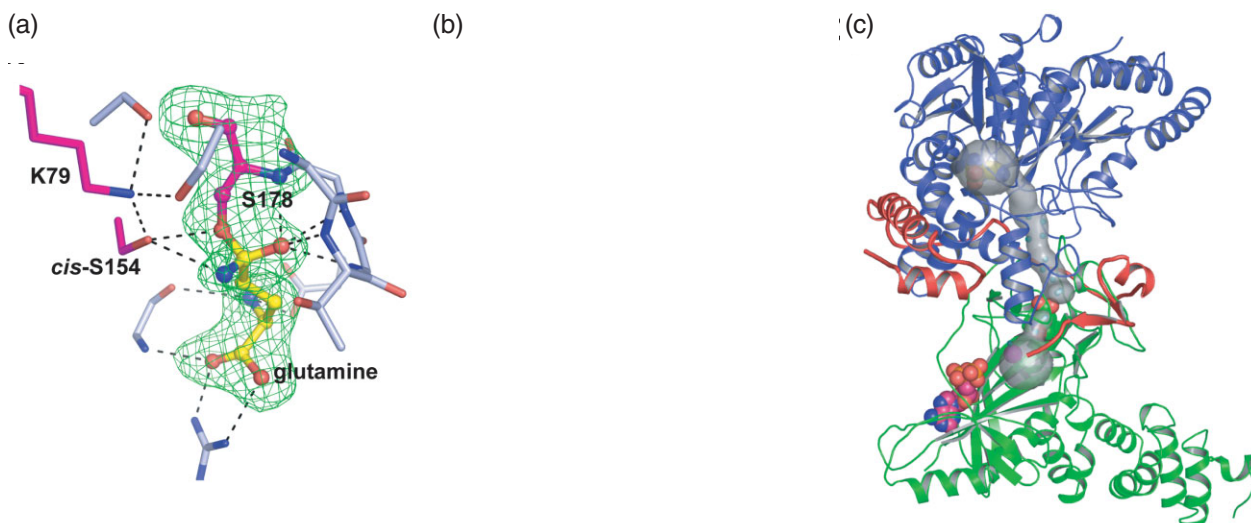


Figure 4

(a) The glutaminase reaction center in GatA is constructed by the conserved catalytic triad (S178, *cis*-S154, and K79, shown as magenta sticks) and residues involved in the hydrogen-bonded network. The *Fo-Fc* electron density map (contoured at  $3\sigma$  and shown as a green mesh) was calculated without including glutamine or S178 in the model.

(b) The ADP in the cradle domain of GatB shown as a stick model, together with the *Fo-Fc* electron density map calculated without the ADP model (contoured at  $2\sigma$  and shown as a blue mesh). Residues contributing to  $Mg^{2+}$  recognitions are shown as stick models with labels.

(c) The intermolecular ammonia channel (gray) calculated for a water-omitted GatCAB/glutamine complex.

A study of the complex structure with ADP revealed the precise position of the ADP binding site to be at the bottom of the cradle domain of GatB (Fig. 4b). The ADP binding pocket is located near the magnesium ion coordinated by the three conserved residues His12, Glu124, and Glu150. These results demonstrate that a kinase and transamidase reactions center is located in the bottom of the cradle domain.

Unexpectedly, although the glutaminase and transamidase reactions are tightly coupled, the two active sites are separated by 30 Å. However, the two reaction centers in GatA and GatB are connected by an intermolecular channel. In the glutamine-binding structure, this channel is filled with a large amount of solvent molecules, indicating that this is the route by which ammonia travels from GatA to GatB. This ammonia channel is closed by a conserved Glu125 located at its exit, suggesting that glutaminase activity can be down-regulated by clogging of the ammonia channel without Glu-tRNA<sup>Gln</sup> binding. These results suggest that the ammonia channel is opened up by the binding of Glu-tRNA<sup>Gln</sup>, with the glutaminase activity then up-regulated by the flow and consumption of the generated ammonia at GatB.

**A. Nakamura, M. Yao, S. Chimnarong, N. Sakai and I. Tanaka (Hokkaido Univ.)**

#### Reference

- [1] A. Nakamura, M. Yao, S. Chimnarong, N. Sakai and I. Tanaka, *Science*, **312** (2006) 1954.

## 7-3 Complete Crystallographic Analysis of CCA-Adding Dynamics by the Class I CCA-Adding Enzyme

RNA polymerization by template-dependent RNA polymerases is driven by the dynamics of enzyme, the nucleic acid template, and its substrate. However, it has been a mystery how nucleic acid template-free RNA polymerization by nucleic acid template-free RNA polymerases proceeds. In this report, a complete set of snapshots of nucleic acid template-free RNA polymerization by the class-I archeal CCA-adding enzyme is presented (Fig. 5).

Four different mini-helices (CCA-, CA-, A-lacking and mature CCA end, hereafter referred to as mini-D, mini-DC, mini-DCC, and mini-CCA, respectively) and two different NTPs (ATP and CTP) were chosen as substrates to cover all of the CCA-synthesis steps. [Hereafter, the CCA-adding enzyme complexes with mini-D, mini-DC, mini-DCC and mini-CCA are referred as the mini-D, mini-DC, mini-DCC and mini-CCA stages, respectively, and the ternary CCA-adding enzyme complexes with mini-DC and CTP, and mini-DCC and ATP are referred as the miniDC+CTP and mini-DCC+ATP stages, respectively.] Complexes representing several different reaction stages were crystallized, and diffraction data were recorded at AR-NW12A, BL-5A or BL-17A. All of the data were processed using the HKL2000 program, and their structures were solved at resolutions of 2.5-2.85 Å.

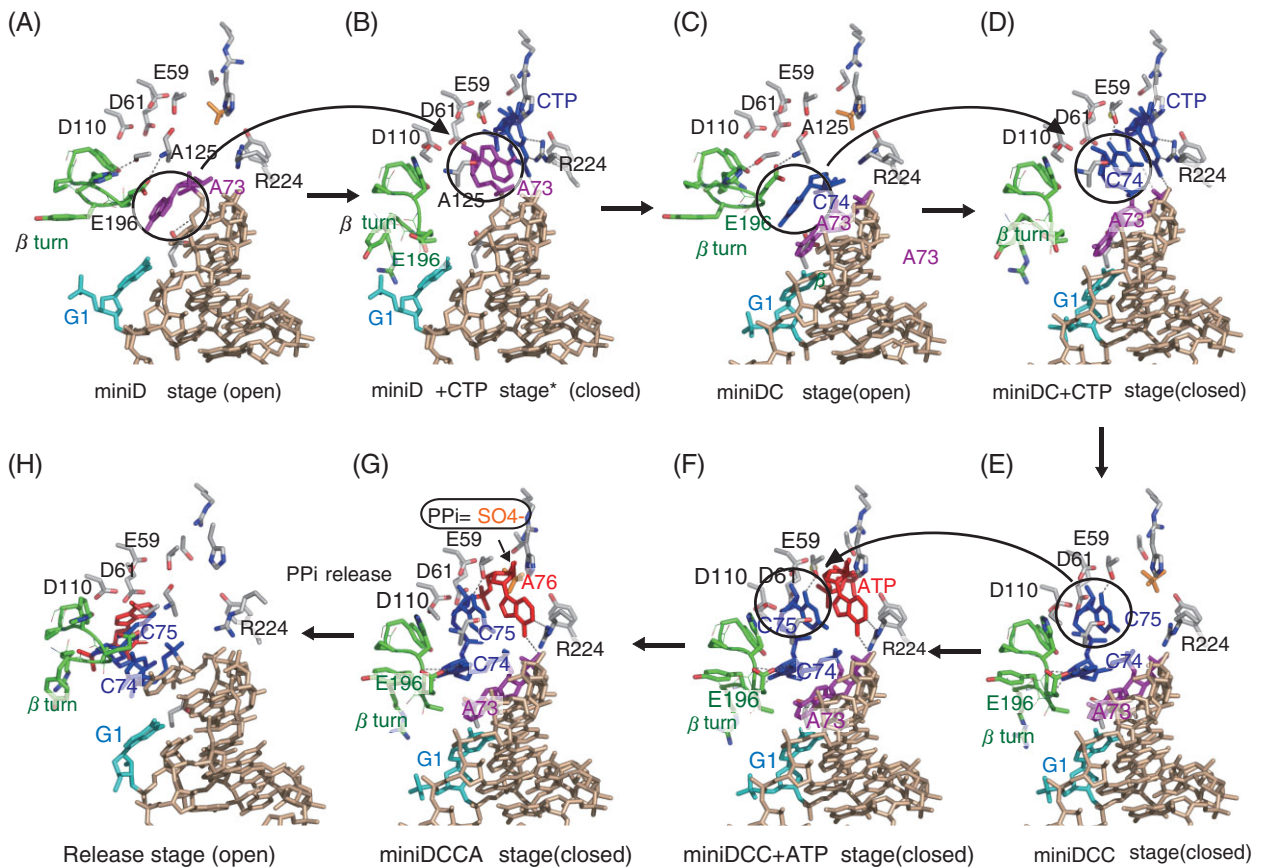


Figure 5

Complete crystallographic analysis of the CCA-adding reaction by the class I CCA-adding enzyme. (A) mini-D stage, (B) mini-D+CTP stage (model), (C) mini-DC stage, (D) mini-DC+CTP stage, (E) mini-DCC stage, (F) mini-DCC+ATP stage, (G) mini-DCCA stage, and (H) release stage.

The catalytic cleft between the NH<sub>2</sub>-terminal and central domain is closed during the transition from the binary mini-DC stage to the ternary mini-DC+CTP stage, inducing a drastic conformational change in the  $\beta$ -turn motif of the NH<sub>2</sub>-terminal domain of the enzyme. This allows the 3'-terminal nucleotide of the RNA primer to flip, and the C-addition to proceed. Therefore, the template for CTP is the dynamics of the enzyme and RNA primer complex, which is induced by an incoming nucleotide. After C-addition, the 3'-end of the primer is back-located to allow the next A-adding reaction to proceed.

On the other hand, no significant conformational change of enzyme is induced during the transition from the binary mini-DCC stage to the ternary mini-DCC+ATP stage. During the A-adding reaction, the enzyme and the 3'-end of RNA are locked, and the enzyme is fixed to the closed conformation. Therefore, the template for ATP is the enzyme and RNA primer complex itself (ribonucleoprotein; RNP). This is distinct to the C-adding reaction, where the dynamics of the enzyme and RNA complex is required. The T $\Psi$ C loop of the RNA primer interacts with the enzyme in the same manner during the CCA-adding reaction, which might prevent the enzyme from undergoing continuous conformational transition for polymerization after CC-addition, thus ensuring the termination of polymerization after the last A-addition.

### K. Tomita (AIST)

#### Reference

- [1] K. Tomita, R. Ishitani, S. Fukai and O. Nureki, *Nature*, **443** (2006) 956.

## 7-4 Crystal Structure of the Complex between Mammalian Eap45 GLUE Domain and Ubiquitin

Ubiquitin (Ub)-dependent protein degradation is an essential down-regulation mechanism for maintaining eukaryotic cells. The downregulation of membrane receptor proteins is triggered by attaching mono-Ub to the receptor proteins [1], whereas soluble proteins to be degraded are modified by a K48-linked poly-Ub chain. The mono-ubiquitinated receptors are sorted on early endosomes and sent to multivesicular bodies for lysosomal degradation with the aid of sorting-machineries such as Hrs/STAM/Eps15, ESCRT-I, ESCRT-II and ESCRT-III complexes [2]. Hrs/STAM/Eps15, ESCRT-I and ESCRT-II interact with Ub and their Ub-binding ability is essential for the mono-Ub mediated protein down-regulation.

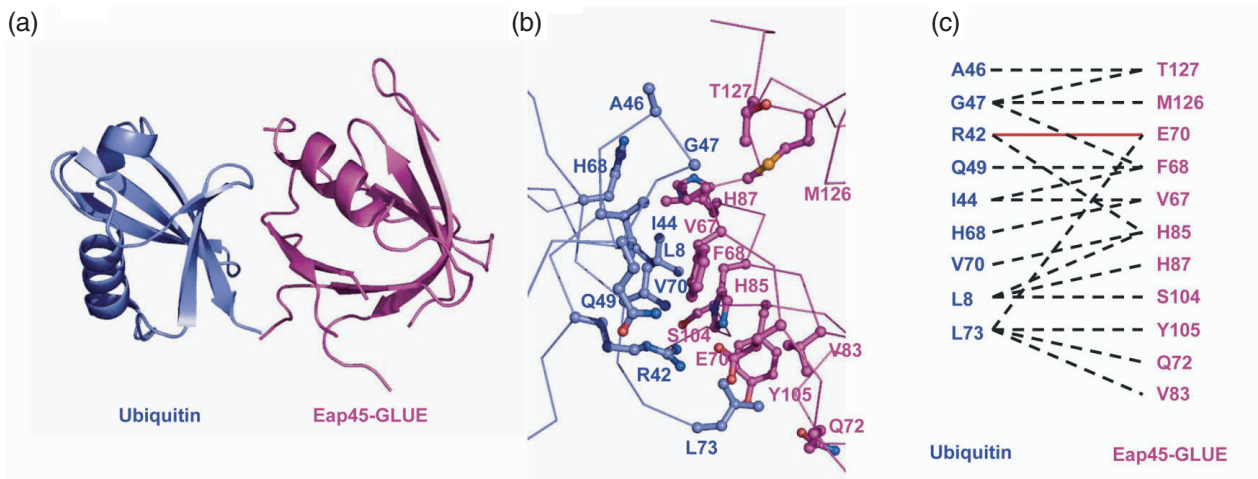


Figure 6

(a) Overall structure of the complex between mouse Eap45 GLUE (magenta) and Ub (blue). (b) Close-up view of the interaction site. Residues involved in the binding are shown as ball-and-stick models with red, blue and orange balls representing oxygen, nitrogen and sulfur atoms, respectively. (c) Schematic diagram of the GLUE-Ub interaction. Dashed black lines indicate hydrophobic and van der Waals contacts between Eap45 GLUE and Ub, and the solid red line indicates a salt bridge.

Among these complexes, mammalian ESCRT-II has a unique Ub-binding domain, the Eap45-GLUE domain, which binds not only to Ub but also to a lipid, phosphatidylinositol (PI), for the localization of ESCRT-II on endosomal membranes [3]. Recently, the crystal structure of its yeast homologue, Vps36-GLUE, was solved and its PI-binding site has been revealed [4]. However, the mechanism of Ub recognition by the Eap45-GLUE domain was still unclear because yeast Vps36-GLUE does not bind to Ub.

In order to reveal the Ub-interaction mechanism of Eap45-GLUE, we crystallized a mouse Eap45-GLUE/Ub complex using the hanging drop vapor-diffusion method, after extensive searches for protein expression, purification and crystallization conditions. Diffraction data sets were collected at BL41XU of the SPring-8, and AR-NW12A and BL-5A of the PF. Although the resolution of the best data set was only 3.35 Å, we were able to solve the structure using the molecular replacement method [5]. Since the resolution was poor, we used a 4.0-Å anomalous dataset of a Se-Met labeled crystal to confirm the methionine positions in Eap45-GLUE, enabling the correct assignment of residues.

The structure of mouse Eap45-GLUE is a PH domain fold, similar to that of the yeast Vps36-GLUE domain (Fig. 6a). The interaction surface of the Ub molecule consists of L8, R42, I44, A46, G47, Q49, H68, V70 and L73, involving the common interaction surface of Ub termed the “I44 surface” (Figs. 6b and 6c). The Ub interacts with V67, F68, E70, V83, Q72, M126, H85, H87, S104, Y105 and T127 of Eap45-GLUE, burying 1000 Å<sup>2</sup> of their accessible surface area (Figs. 6b and 6c). On the center of the interaction surface of Eap45-GLUE, V67, F68 and H85 form a characteristic hydrophobic patch, which interacts with the Ub I44 surface consisting of L8, I44, H68 and V70. In addition to the hydrophobic interactions, Eap45-GLUE E70 is involved

in electrostatic interactions with Ub R42. We also performed a Ub-binding assay with several Eap45-GLUE mutants and confirmed that V67, F68, E70 and H85 are actually involved in the Ub-binding.

Importantly, the revealed Ub-binding site of Eap45-GLUE is located at a completely different position from the expected PI binding site (Fig. 7), suggesting that Eap45-GLUE binds to Ub and PI simultaneously. As the yeast Vps36 has also been shown to bind Ub and IP independently [5], the simultaneous-binding ability of Eap45-GLUE to Ub and the endosomal membrane is expected to be essential for the downregulation of membrane proteins.

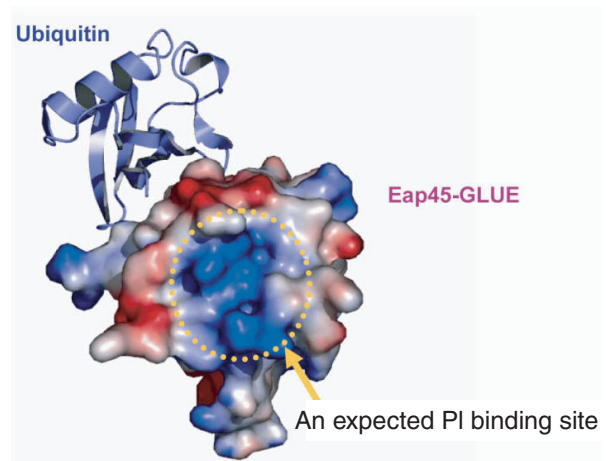


Figure 7

Electrostatic potential surface of the phosphoinositide binding side of the Eap45-GLUE domains. The predicted PI binding site, which is the corresponding site to the PI binding site of the yeast Vps36-GLUE domain [5], is indicated by a dashed yellow circle, and the Ub molecule is shown as a ribbon model.

S. Hirano<sup>1</sup>, N. Suzuki<sup>1</sup>, M. Kawasaki<sup>1</sup>, T. Slagsvold<sup>2</sup>, D. Trambaiolo<sup>1</sup>, R. Kato<sup>1</sup>, H. Stenmark<sup>2</sup> and S. Wakatsuki<sup>1</sup> (<sup>1</sup>KEK-PF, <sup>2</sup>The Univ. of Oslo)

## References

- [1] C. Raiborg and H. Stenmark, *Cell Struct. Funct.*, **27** (2002) 403.
- [2] C. Raiborg, T.E. Rusten and H. Stenmark, *Curr. Opin. Cell Biol.*, **15** (2003) 446.
- [3] T. Slagsvold, R. Aasland, S. Hirano, K.G. Bache, C. Raiborg, D. Trambaiolo, S. Wakatsuki and H. Stenmark, *J. Biol. Chem.*, **280** (2005) 19600.
- [4] H. Teo, D.J. Gill, J. Sun, O. Perisic, D.B. Veprintsev, Y. Vallis, S.D. Emr and R.L. Williams., *Cell*, **125** (2006) 99.
- [5] S. Hirano, N. Suzuki, T. Slagsvold, M. Kawasaki, D. Trambaiolo, R. Kato, H. Stenmark and S. Wakatsuki, *Nature Struct. Mol. Biol.*, **13** (2006) 1031.

## 7-5 Studies of the Recognition Mechanism of Small GTPase Rab11 by FIP3

Small GTPases belonging to the Ras-like superfamily regulate endocytotic membrane trafficking, and ARF and Rab proteins participate in multiple stages of trafficking along the exocytic and endocytic pathways. ARFs initiate the budding of coated carrier vesicles by recruiting coat protein complexes onto donor membranes, whereas Rabs regulate the targeting and docking/fusion of vesicles with acceptor membranes [1]. The Rab proteins constitute the largest family of small GTPases, with more than 60 known for mammals [2]. The Rab11 regulates the recycling of endosomes to the plasma membrane via interactions with the Rab11 family of interacting proteins (FIP). These proteins have highly conserved Rab binding domains (RBD) at their C termini. To better understand the recognition mechanisms of Rab11 by members of its FIP, we have determined the crystal structure of Rab11 in complex with the RBD of FIP3 [3].

We attempted to crystallize the RBD of a FIP3 fragment (715-756; hereafter FIP3-RBD) in complex with a C-terminally truncated form of Rab11(Q70L) (residues 1-173; hereafter called Rab11). We succeeded in obtaining complex crystals using 20% isopropanol, 3-5% (w/v) PEG 4000, and 0.05 M MES-NaOH pH 5.8-6.0. Initial phases were determined using selenomethionine-substituted proteins by the multiple anomalous dispersion method, and the structure was refined to a spatial resolution of 1.75 Å using BL-6A and AR-NW12A. In the asymmetric unit, there are two Rab11 and two FIP3-RBD molecules (Fig. 8). Each FIP3-RBD consists of an N-terminal long  $\alpha$ -helix (residues 716-748) followed by a 90 degree bend at the conserved Pro750 residue, a  $3^{10}$  helix (residues 750-752) and a C-terminal short  $\beta$ -strand (residues 753-755), adopting an 'L' shape. The long  $\alpha$ -helix is amphiphilic, forms a parallel coiled-coil homodimer, and symmetrically interacts with two Rab11 molecules on both sides, forming a quaternary Rab11-(FIP3-RBD)<sub>2</sub>-Rab11 complex (Fig. 8). The Rab11 recognition region of FIP3-RBD can be divided into three regions: (i) switch 1, (ii) switch 2 and (iii) interswitch (Fig. 9).

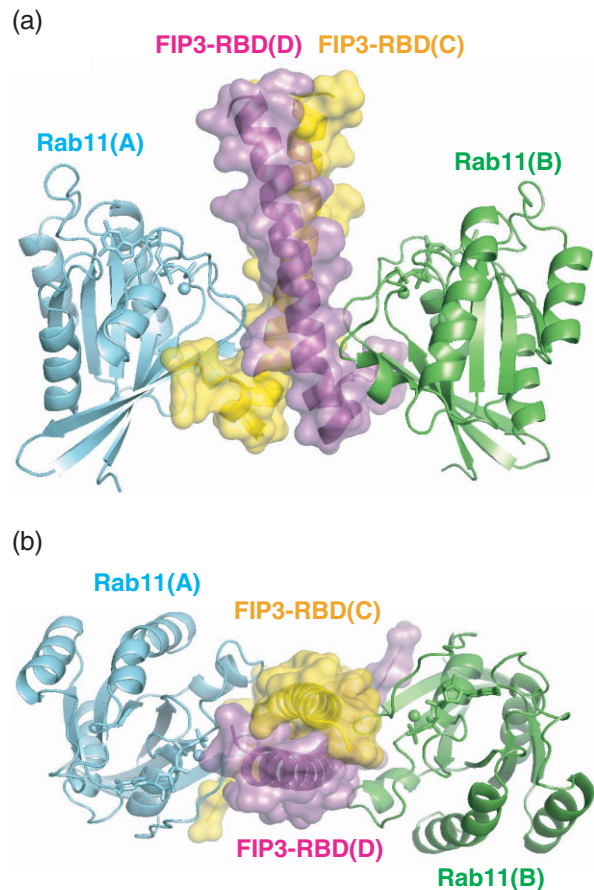


Figure 8  
Crystal structure of the Rab11-FIP3-RBD complex. (a) Ribbon diagram of the complex (side view). The asymmetric unit contains two Rab11 molecules (A; cyan and B; green) and two FIP3-RBD molecules (C; yellow and D; purple). GTP and Mg<sup>2+</sup> ions are shown as ball-and-stick models. (b) Top view of (a).

### (i) Switch 1 (Fig.9a)

In the middle of the FIP3-RBD the amphiphilic  $\alpha$ -helix is involved in binding the switch 1 region of the Rab11 molecule. The interaction is hydrophobic in nature with the Tyr737<sup>D</sup> (the superscript D denotes a residue of the FIP3-RBD in chain D) side chain of FIP3-RBD packing against Gly45 of Rab11, and the side chain of Leu734<sup>D</sup> and the aliphatic portion of the Arg733<sup>D</sup> side chain interacting with the side chain of Rab11 Ile44.

### (ii) Switch 2 (Fig9b)

The hydrophilic side of the amphiphilic helix of FIP3-RBD interacts with the switch 2 region of the Rab11 molecule. The side chains of Arg74 and Arg82 in switch 2 form salt bridges with Asp739 and Glu747, respectively. Another remarkable feature in the switch 2 region of Rab11 is that the side chain of Tyr80 points inward, forming an intramolecular hydrogen bond with the main chain carbonyl of Leu16. As a result, Rab11 forms a characteristic large hydrophobic pocket surrounded by the Ile76, Ala79, and Tyr80 of the switch 2 region and Trp65 of the interswitch region, which accommodates the large side chain of FIP3-RBD Met746.

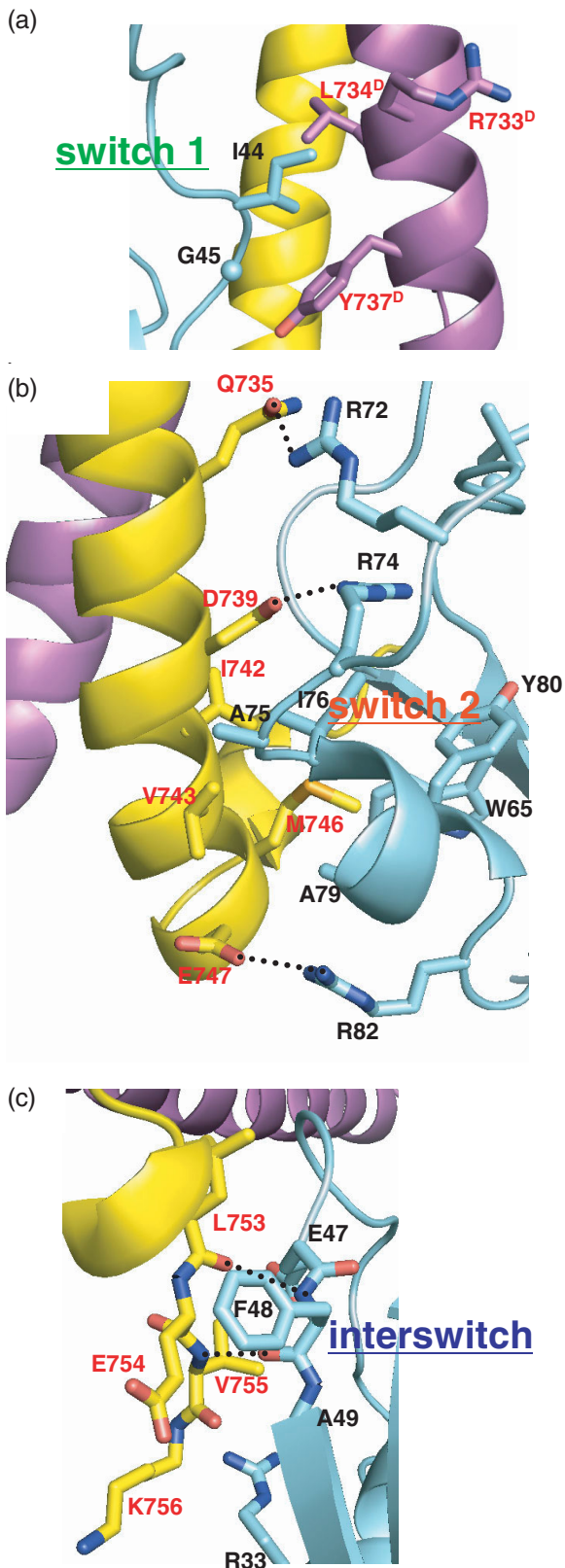


Figure 9  
Interaction between Rab11 and FIP3-RBD. Close up views of the (a) switch 1, (b) switch 2 and (c) interswitch regions of Rab11 in complex with FIP3-RBD. The color schemes are the same as those of Fig. 8. The residues involved in the interaction are labeled and indicated by ball-and-stick models. The black dashed lines indicate hydrogen bonds or electrostatic interactions.

(iii) *Interswitch* (Fig. 9c)

An intermolecular parallel  $\beta$ -sheet is formed between the C-terminal short  $\beta$ -strand of FIP3-RBD and the  $\beta$ 2 strand of the Rab11 interswitch region; the main chains of Leu753 (carbonyl oxygen) and Val755 (amide nitrogen) of FIP3-RBD form hydrogen bonds with the main chain of Phe48 (amide nitrogen and carbonyl oxygen) of Rab11. These recognition mechanisms of FIP3 are quite different from those of other GTPase effectors.

T. Shiba<sup>1,2</sup>, H. Koga<sup>3</sup>, H.-W. Shin<sup>3</sup>, M. Kawasaki<sup>1</sup>, R. Kato<sup>1</sup>, K. Nakayama<sup>3</sup> and S. Wakatsuki<sup>1</sup> (<sup>1</sup>KEK-PF, <sup>2</sup>The Univ. of Tokyo, <sup>3</sup>Kyoto Univ.)

References

- [1] P. Chavrier and B. Goud, *Curr. Opin. Cell Biol.*, **11** (1999) 466.
- [2] M. Zerial and H. McBride, *Nature Rev. Mol. Cell Biol.*, **2** (2001) 107.
- [3] T. Shiba, H. Koga, H.-W. Shin, M. Kawasaki, R. Kato, K. Nakayama and S. Wakatsuki, *Proc. Natl. Acad. Sci.*, **103** (2006) 15416.

## 7-6 The Structural and Chemical Basis of Protein Disulfide Bond Formation in *E. Coli*

Many secretory proteins undergo oxidative folding, in which they acquire intra- or intermolecular disulfide bonds. The periplasmic space of *E. coli* contains a series of Dsb enzymes, which catalyze the introduction and isomerization of protein disulfide bonds (Fig. 10). DsbA is the primary disulfide bond donor, having Cys30-Cys33 disulfide at the active site. It is kept in an oxidized and active state by the cytoplasmic membrane protein DsbB, which transmits electrons from DsbA to ubiquinone (UQ).

To achieve a deep understanding of this disulfide-introducing oxidative system, we determined the crystal structure of a disulfide-linked DsbB-DsbA complex with endogenous UQ [1]. The 3.7 Å resolution structure was complemented with engineered selenomethionine (SeMet) signals to enable structural refinement and consequent illumination of the reaction mechanisms. Data collection for complexes with DsbB(Met36Ala) and DsbB(Met93Ala) variants was carried out at the AR-NW12A of the PF, and other diffraction data sets were collected at the BL44XU of the SPring-8. The crystallographic data reveals that DsbB contains four TM helices arranged into a four-helix bundle configuration (Fig. 11). In addition to the TM helices, a short helix with a horizontal axis exists in the second periplasmic loop of DsbB.

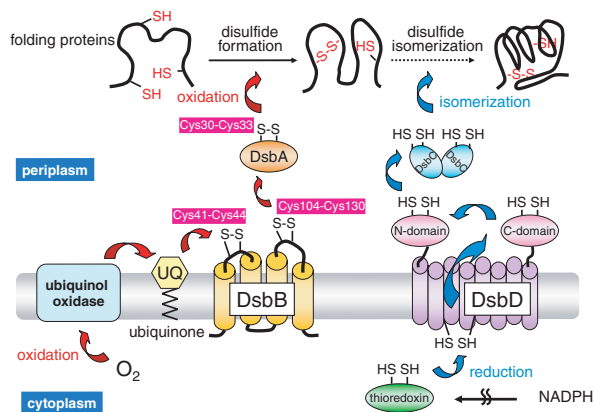


Figure 10  
Dsb enzymes responsible for protein disulfide bond formation in *E. coli*.

One of the important findings in this work is that the UQ-binding site of DsbB is present at the N-terminal end of TM2 (Fig. 11). This is consistent with our recent biochemical insights; the formation of the Cys44-UQ charge transfer (CT) complex and its enhancement by Arg48 during the DsbB catalysis of DsbA oxidation. The area of DsbB which has UQ lined up with Cys41, Cys44 and Arg48 can be regarded as the reaction center, where disulfide bonds are generated *de novo* following the chemical scheme shown in Fig. 11.

It is also noteworthy that conformational change is induced in the periplasmic loop of DsbB by association

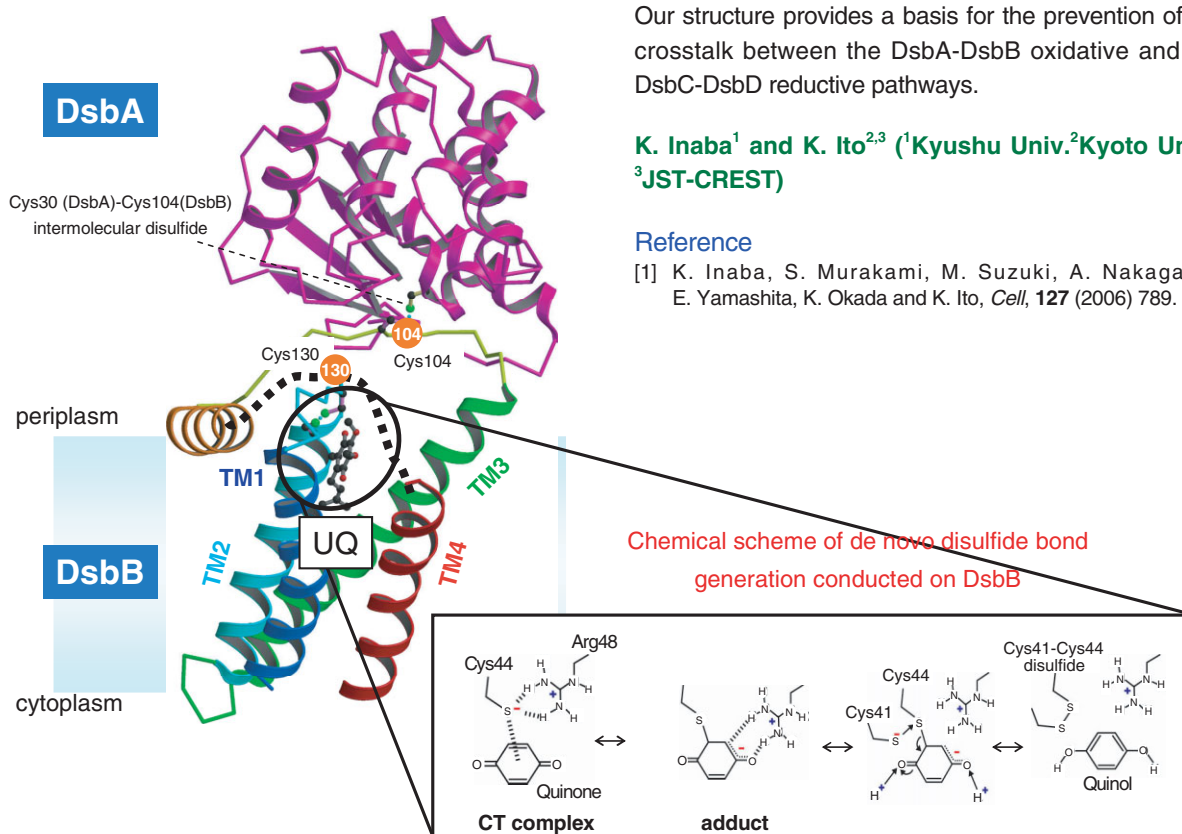


Figure 11  
Crystal structure of the DsbA-DsbB-ubiquinone (UQ) complex.

with DsbA. DsbB in isolation usually contains two intra-molecular disulfide bonds – between Cys41 and Cys44 and between Cys104 and Cys130. Strikingly, residue 130 of DsbB in the complex structure was separated from Cys104 beyond the range (~2 Å) of disulfide bond formation. This separation is ascribable to the capture of the Cys104-containing DsbB segment by the deep groove of DsbA. We envisage that such DsbA-induced cysteine relocation should prevent the reverse reaction caused by the backward attack by Cys130 against the Cys30 (DsbA)-Cys104 (DsbB) intermolecular disulfide bond. Moreover, Cys130 has proved to reside very close to the Cys41-Cys44 pair, which must be advantageous for physiological electron flow from the Cys104-Cys130 pair to the Cys41-Cys44 pair. Thus, we propose that DsbB is transformed into a superoxidizing enzyme when it encounters a specific substrate – DsbA.

In addition to the disulfide-introducing oxidative pathway, *E. coli* has a disulfide-isomerizing reductive pathway relating to DsbC, DsbD and cytoplasmic thioredoxin (Fig. 10). While DsbC exists in the same cellular compartment as DsbA and possesses a thioredoxin fold similar to that of DsbA, it is kept in a reduced state by the action of DsbD. DsbC must not be oxidized by DsbB to avoid futile cycles of electron transfer from DsbD to DsbB via DsbC. Unlike DsbA, DsbC forms a homodimer. Notably, superimposition of one of its thioredoxin domains on the DsbB-DsbA complex in such a way as to minimize RMSD resulted in a clash of the other protomer onto the membrane surface. Thus, DsbC would have a serious steric problem if it were to bind DsbB. Our structure provides a basis for the prevention of the crosstalk between the DsbA-DsbB oxidative and the DsbC-DsbD reductive pathways.

K. Inaba<sup>1</sup> and K. Ito<sup>2,3</sup> (<sup>1</sup>Kyushu Univ.<sup>2</sup>Kyoto Univ.,<sup>3</sup>JST-CREST)

#### Reference

- [1] K. Inaba, S. Murakami, M. Suzuki, A. Nakagawa, E. Yamashita, K. Okada and K. Ito, *Cell*, **127** (2006) 789.



## 7-7 Structure of the Insulin Receptor Ectodomain Homodimer

The insulin receptor (IR) is a phylogenetically ancient tyrosine kinase receptor found in organisms as primitive as cnidarians and insects. In higher organisms it is essential for glucose homeostasis. Here we present the crystal structure of the IR-A ectodomain homodimer, complexed with four Fabs from the monoclonal antibodies [1]. The structure reveals the way in which the multiple domains in the insulin receptor dimer are organized, identifies the elusive second binding site on the receptor and suggests how the high-affinity insulin-receptor complex, which leads to signal induction, is generated.

Crystals of IR  $\Delta\beta$  protein construct binding insulin with similar affinity as intact ectodomain with Fab 83-7 and 83-14 were produced by vapour. Native data sets were collected from single crystals up to 3.8 Å (set 1)



**Figure 12**  
Tube diagram of the IR  $\Delta\beta$  ectodomain homodimer. Individual domains are coloured as follows: L1 - brown, CR - yellow, L2 - green, FnIII-1 - magenta, FnIII-2 - cyan and FnIII-3 - blue.

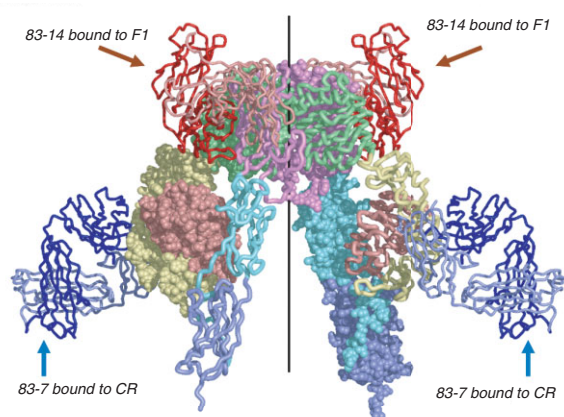


**Figure 13**  
Schematic diagram of the IR  $\Delta\beta$  ectodomain homodimer with the attached pairs of Fabs. The IR homodimer is depicted with a single molecule in tube representation and the other in atomic sphere representation. Domains are coloured as in Fig. 12. The Fab fragments are marked and represented as thin tubes and coloured as follows: 83-7 heavy chain: dark blue, 83-7 light chain: light-blue, 83-14 heavy chain: red, and 83-14 light chain: pink.

and later up to 3.4 Å (set 2) resolution at BL-5A. The space group was C222<sub>1</sub>, with unit cell dimensions  $a = 123.0$  Å,  $b = 319.7$  Å and  $c = 204.9$  Å. Structure was solved using a combination of phases derived from similar fragment of L1-CR-L2 [2] (see below) and single isomorphous replacement phases obtained by a PIP derivative data set (collected earlier at the APS IMCA-CAT 17-ID at 5.5 Å) processed with SHARP followed by iterative cycles of BUSTER-TNT and REFMAC5 and manual model building using XtalView/Xfit. The asymmetric unit comprises one ectodomain  $\alpha$ - $\beta$ -chain pair (*i.e.* the IR  $\Delta\beta$  monomer), one 83-7 Fab and one 83-14 Fab. The IR  $\Delta\beta$  monomer is paired within the unit cell to form the disulphide-bonded IR ectodomain homodimer (Fig. 12 and 13), which arises from a two-fold rotation of the monomer. Each IR ectodomain monomer contains a leucine-rich repeat domain (L1), a cysteine-rich region (CR) and a second leucine-rich repeat domain (L2), followed by three fibronectin type III domains (FnIII-1, -2 and -3). FnIII-2 contains an insert domain (ID) of 120 residues, within which lies the  $\alpha$ - $\beta$  cleavage site. The ID is mostly disordered in the structure. Each  $\alpha$ - $\beta$  monomer has an inverted “V” layout with respect to the cell membrane. One leg of the V is formed by the L1, CR and L2 domains and the other by an extended linear arrangement of the three FnIII domains. At the apex of the inverted V lies the connection between L2 and FnIII-1, which are not in extensive contact within the monomer (516 Å<sup>2</sup> buried molecular surface per interacting pair of L2/FnIII-1 domains). The arrangement of the L1, CR and L2 domains observed here is similar though not identical to that observed earlier for the human IR [2] and IGF1-R [3] L1-CR-L2 fragment structures. The structure (Fig. 12) reveals for the first time the domain arrangement in the disulphide-linked ectodomain homodimer and shows that it adopts a folded-over conformation which places the ligand-binding regions in juxtaposition. This arrangement is very different from previous models. It shows the two L1 domains to be on opposite sides of the dimer, too far apart to allow insulin to bind both L1 domains simultaneously. Instead, the structure implicates the C-terminal surface of the first fibronectin-III domain as the second binding site involved in high-affinity binding.

### V. Streltsov (CSIRO)

#### References

- [1] N. McKern, M. Lawrence, V. Streltsov, M. Lou, T. Adams, G. Lovrecz, T. Elleman, K. Richards, J. Bentley, P. Pilling, P. Hoyne, K. Cartledge, T. Pham, J. Lewis, S. Sankovich, V. Stoichevska, E. Da Silva, C. Robinson, M. Frenkel, L. Sparrow, R. Fernley, V. Epa and C. Ward, *Nature*. **443** (2006) 218.
- [2] M. Lou, T. Garrett, N. McKern, P. Hoyne, V. Epa, J. Bentley, G. Lovrecz, L. Cosgrove, M. Frenkel and C. Ward, *PNAS*, **103** (2006) 12429.
- [3] T. Garrett, N. McKern, L. Meizhen, M. Frenkel, J. Bentley, G. Lovrecz, T. Elleman, L. Cosgrove and C. Ward, *Nature*. **394** (1998) 395.

## 7-8 Dispositional and Conformational Changes of Myosin Crossbridges in Skeletal Muscle Contraction and Regulation Studied Using X-Ray Fiber Diffraction

Energy transduction in muscle contraction is carried out by the asynchronous interaction of two kinds of motor proteins – actin and myosin, powered by the hydrolysis of ATP (Fig. 17E). The two proteins self-assemble into the helical filaments of the sarcomere, the repeating functional unit in striated muscle (Fig. 14). The high degree of order within these filament assemblies allows the recording of detailed X-ray diffraction patterns from

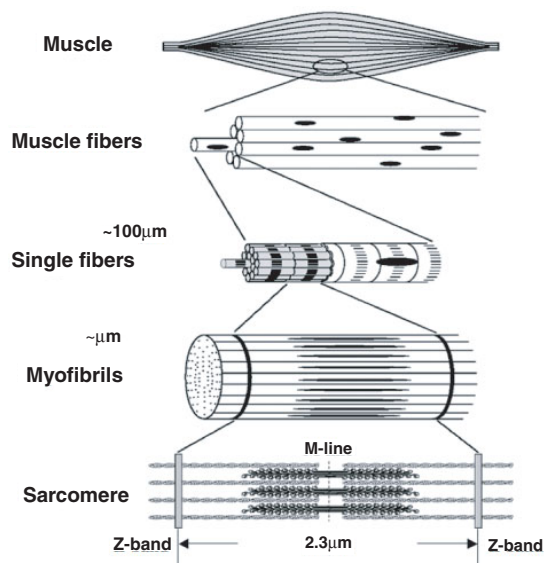


Figure 14  
The hierarchical structure of skeletal muscle.

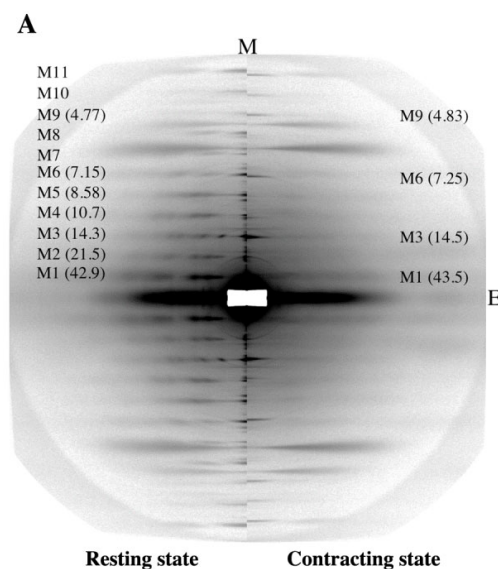


Figure 15  
A. X-ray diffraction patterns in the resting and contracting states of live frog skeletal muscles with their meridional axes coincident. M1 to M11 denote the first to the eleventh order myosin-based reflections with a crystallographic period of 42.9 nm (the resting state) or 43.5 nm (the contracting state). M and E indicate the meridional and equatorial axes, respectively. B. Axial intensity distributions on the meridian in the resting (red) and contracting states (blue). Axial profiles of a series of myosin meridional reflections (M2-M6) are finely sampled (data recorded at the APS) [1].

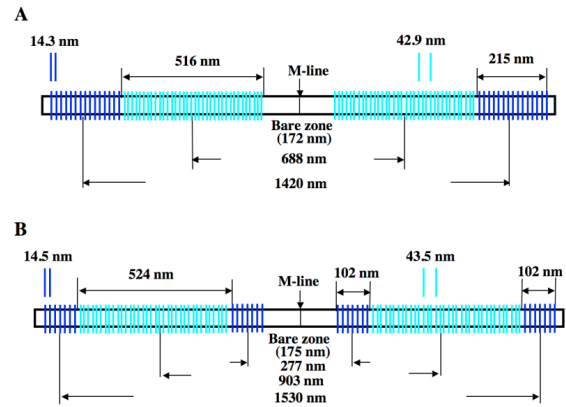
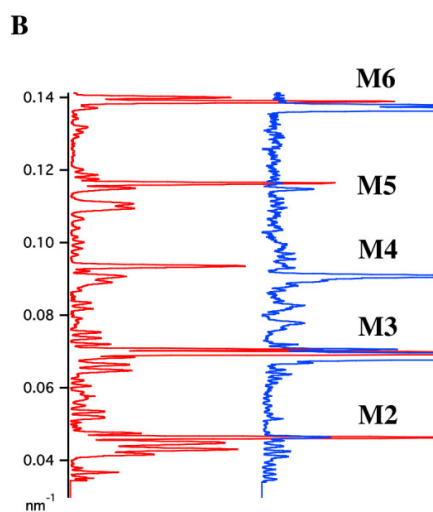


Figure 16  
Distributions of the triplet repeating region (blue) and the singlet repeating region (cyan) of myosin crossbridge arrays along the thick filament across the M-line in the sarcomere, derived from the optimal models of the thick filament. A. The model in the resting state. B. The model in the contracting state.

muscle, providing therefore an indispensable tool for obtaining direct information on the molecular mechanisms underlying muscle contraction.

The dispositional and conformational changes of the myosin crossbridges along thick filaments were investigated at BL-15A by recording X-ray fiber diffraction patterns during contraction of live skeletal muscle under isometric conditions [1, 2]. As can be seen in Fig. 15A, a series of strong reflections indexing on a basic period of 42.9 nm or 43.5 nm on the meridian were observed. These reflections are produced by the presence of a systematic perturbation of the three successive myosin crossbridge repeats within the basic period. In addition, the meridional reflections are finely sampled in the axial direction due to the mirror-image structure of myosin filaments across the M-line in the sarcomere (Fig. 15). With the help of high-angular resolution data recorded at the APS [1], a detailed analysis of axial sampling



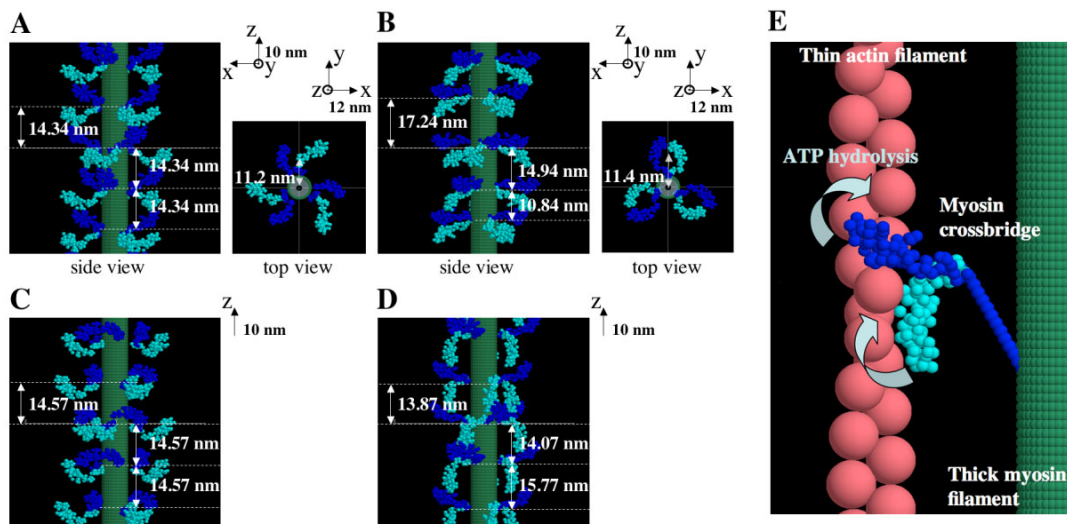


Figure 17

Configurations of myosin crossbridges along the thick filament. A and B show the optimal models in the singlet and triplet repeating regions, respectively, in the resting state. C and D show those in the singlet and triplet regions, respectively, in the contracting state. In A-D, the z-axis is orientated in the direction of the Z-band in the sarcomere, and is parallel to the filament axis. E. Schematic diagram of the interaction of myosin heads and actin, coupled with the hydrolysis of ATP in contracting muscle. The pink balls represents a thin actin filament, and the two sets of blue and cyan balls represent the two heads of a myosin crossbridge with an S2 portion (shown as a blue stick). The thick filament backbone (green) is indicated as a structure-less cylinder.

periods on the meridional reflections showed that there existed a mixed population of crossbridge arrangements along the thick filament – a triplet repeating region and a singlet repeating region (Fig. 16) [1, 2]. In both resting (Fig. 16A) and contracting (Fig. 16B) states, the triplet region was on the central part of half of the thick filaments and occupied about 70% of the total length of the myosin crossbridge arrangement along the filaments.

High-resolution modeling using the crystallographic structure of a myosin head revealed that the two heads of a crossbridge around the backbone were axially tilted in opposite directions along the three-fold helical tracks of myosin filaments (Fig. 17) [2]. In the resting state, one crossbridge head appeared to be in close proximity to the other head at the adjacent crossbridge level in the axial direction in the singlet region (Fig. 17A). In the top view, the two crossbridge heads appeared to be flared, forming a windmill-like shape. In the triplet region, this contact between myosin heads occurred only between narrower inter crossbridge levels (Fig. 17B), and in the top view one crossbridge head came into contact with its partner head at their outer ends, making a U-shaped structure at the same axial level. These results show that head-head interactions of myosin crossbridges occur and may provide a switching-off mechanism for the actomyosin interaction in the resting state. During contraction, in either the singlet (Fig. 17C) or triplet (Fig. 17D) regions one head of an interacting crossbridge was oriented more perpendicular to the actin filaments than the partner head. This feature became more prominent in the triplet region (Fig. 17D); the partner heads appeared to be greatly flared axially. These results lead to the concept that two heads of a myosin crossbridge may play alternate roles for the generation of contractile force (Fig. 17E); the heads that appeared to be axially flared may represent an average conformation over the

heads cycling at different times, and the more perpendicularly inclined heads may be in a pre-force producing state, weakly bound to actin. In addition to the thin filament-based regulation, myosin-mediated regulation also needs to be considered in the contraction of vertebrate striated muscle.

**K. Oshima<sup>1</sup>, Y. Takezawa<sup>1</sup>, Y. Sugimoto<sup>1</sup>, T. Kobayashi<sup>2</sup>, T. C. Irving<sup>3</sup> and K. Wakabayashi<sup>1</sup>, (<sup>1</sup>Osaka Univ., <sup>2</sup>Shibaura Inst. Tech., <sup>3</sup>Illinois Inst. Tech.)**

#### References

- [1] K. Oshima, Y. Takezawa, Y. Sugimoto, T. Kobayashi, T.C. Irving and K. Wakabayashi, *J. Mol. Biol.*, **367** (2007) 275.
- [2] K. Oshima, Y. Takezawa, Y. Sugimoto, T.C. Irving and K. Wakabayashi, *Fiber Diffraction Rev.*, **13** (2005) 23.

## 7-9 Low-Dose Hypersensitivity in Nucleus-Irradiated V79 Cells Studied Using a Synchrotron X-Ray Microbeam

Low-dose hyper radiosensitivity (HRS) is a phenomenon in which cells show higher sensitivity to ionizing radiation in the low-dose region (below ~0.5 Gy) than for higher doses. The phenomenon plays a very important role in determining biological effects in the low-dose region. During a study of biological responses in the low-dose region using an X-ray microbeam irradiation system with synchrotron radiation as the light source at BL-27B, we found that the magnitude of HRS depends on the part of the cell which is irradiated. This microbeam irradiation system [1, 2] can be used to irradiate target cells one by one, using a monochromatic 5.35-keV

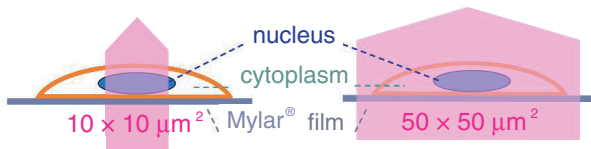


Figure 18  
Schematic diagram of nucleus irradiation (left) and whole cell irradiation (right). Both nucleus and cytoplasm were irradiated with the  $50 \times 50 \mu\text{m}^2$  beam, while only the nucleus was irradiated with the  $10 \times 10 \mu\text{m}^2$  beam.

X-ray beam of arbitrary size. The smallest possible beam size is  $5 \times 5 \mu\text{m}^2$ . This study takes advantage of these characteristics of the system, and we have compared the dose-survival relationship of mammalian cells for X-ray microbeams of different sizes.

Differences in lethal effects of different size microbeams were studied for Chains hamster lung V79 cells. The beam sizes we employed were  $10 \times 10 \mu\text{m}^2$  targeted at part of the nucleus, and  $50 \times 50 \mu\text{m}^2$  targeted at the whole cell (Fig. 18). When the cell nuclei were irradiated with the  $10 \times 10 \mu\text{m}^2$  X-ray beam, the survival fraction was almost the same as that for the  $50 \times 50 \mu\text{m}^2$  beam, except in the low-dose region. In the low-dose region, HRS was more clearly observed in the nucleus-irradiated cells, and the survival curve exhibited a minimum of about 60% at 0.5 Gy, as shown in Fig. 19 [3, 4].

In studies of the cell cycle (Fig. 20) dependence of lethality, cells irradiated during the  $G_2$  phase have been reported to exhibit more distinctive HRS than cells irradiated in either the  $G_1$  or S phases [5]. This is explained as follows: Cells irradiated during the  $G_2$  phase which receive only minor DNA damage proceed to the M (mitosis) phase, passing through the  $G_2$  checkpoint, at which cell cycle progression stops when metabolic processes in  $G_2$  phase is not normally accomplished, leading to cell death during mitosis due to unrepaired DNA damage. More significant DNA damage produced with a higher dose is recognized at the  $G_2$  checkpoint and the cell stops proceeding with cell cycle ( $G_2$  arrest). This allows cells to secure time for repair. As a result, HRS is observable in the dose-survival curve. In our experiment, we cannot ascribe differences in the magnitude of HRS to cell stage in the irradiated populations, since the cell populations were asynchronous in our experiments. The only difference in experimental conditions was the irradiated domain of the cell, with either the entire cell or only the nucleus being irradiated. The amount of energy deposition in the nucleus was almost equal for both irradiations when compared at the same nuclear-averaged dose. These results suggest that energy deposition in the cytoplasm may play an important role in cell lethality in the low-dose region through intracellular signaling.

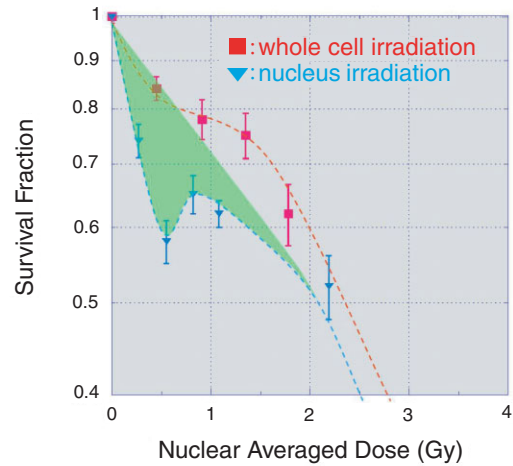


Figure 19  
Dose-survival curves of V79 cells irradiated with  $10 \times 10$  (▼) and  $50 \times 50$  (■)  $\mu\text{m}^2$  X-ray beams. Cell killing is enhanced in the absence of energy deposition to the cytoplasm, as shown by the green region in the figure. The dotted lines were drawn by eye in consideration of the high-dose region data (not shown).

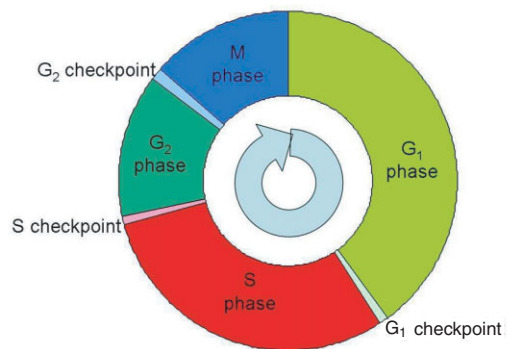


Figure 20  
Schema of cell cycle and cell cycle checkpoints. The reproductive cycle of a cell, between one division and the next, is termed the cell cycle. The period for DNA synthesis is called the S phase, the period during which cell division (mitosis) occurs is called the M phase, and the gap periods between S and M are called  $G_1$  and  $G_2$ . During the cell cycle, there are several checkpoints at which progression can be arrested if the preceding stage has not been completed normally. These arrests are considered to serve the purpose of securing time for errors to be repaired in order to prevent disaster occurring during the subsequent stage of the cycle.

M. Maeda, N. Usami and K. Kobayashi (KEK-PF)

## References

- [1] K. Kobayashi, N. Usami, K. Hieda, K. Takakura, H. Maezawa and T. Hayashi, *Nucl. Instrum. Methods. Phys. Res. A.*, **467-8** (2001) 1329.
- [2] K. Kobayashi, N. Usami, H. Maezawa, T. Hayashi, K. Hieda and K. Takakura, *J. Biomed. Nanotechnol.*, **2** (2006) 1.
- [3] M. Maeda, N. Usami and K. Kobayashi, *Radiat. Res.*, **166** (2006) 679.
- [4] M. Maeda, N. Usami and K. Kobayashi, "Low-dose Hypersensitivity in Nucleus-irradiated V79 Cells Studied with Synchrotron X-ray Microbeam" *J. Radiat. Res.*, (2007) Accepted.
- [5] S.C. Short, M. Woodcock, B. Marples and M.C. Joiner, *Int. J. Radiat. Biol.*, **79** (2003) 99.